RSC Advances

ROYAL SOCIETY OF CHEMISTRY

www.rsc.org/advances

RSC Advances

Single-phase nickel-doped ceria cathode with *in-situ* grown nickel nanocatalyst for direct high-temperature carbon dioxide electrolysis

Wentao Qi [a], Kui Xie [a, b] *, Min Liu [a], Guojian Wu [a], Yan Wang [a], Yong Zhang [a], Yucheng Wu [a, b] *

Received (in XXX, XXX) Xth XXXXXXXXX 20XX, Accepted Xth XXXXXXXXX 20XX
DOI: 10.1039/b000000x

This paper reports the *in-situ* growth of Ni nanocatalysts to anchor onto the CeO_2 surface to combine the surface oxygen vacancy and form heterogeneous catalysis sites with the aim of improving electrocatalytic activity through direct exsolution of Ni nanoparticles from Ni-doped CeO_2 lattice in a reducing atmosphere at higher temperatures. The combination use of XRD, TEM, SEM and XPS confirms the *in-situ* exlosution of Ni nanoparticles on CeO_2 surface. The doping of CeO_2 with nickel leads to a charge redistribution and an increase of oxygen vacancy concentration. The electrical properties of $Ce_{1-x}Ni_xO_2$ (x=0, 0.05, 0.10, 0.15 and 0.20) are systematically investigated and correlated to their electrochemical performance in symmetrical and electrolysis cells. The electrical properties and electrochemical performances improve with increasing Ni contents. The $Ce_{0.85}Ni_{0.15}O_2$ cathode with anchored Ni nanocrystal shows the best electrochemical performances for carbon dioxide electrolysis with reasonable short-term stability; however, the electro-catalytic activity of $Ce_{0.8}Ni_{0.2}O_2$ with excess Ni particles on surface rapidly decays because of adverse agglomeration of Ni particles at high temperatures.

Introduction

Solid oxide electrolysers have been attracting widespread attentions because of their tremendous advantages of efficient conversion of carbon dioxide into fuels using renewable electrical energy [1-3]. An oxide-ion-conducting solid oxide electrolyser can directly electrolyze carbon dioxide into carbon monoxide and oxygen. Carbon dioxide molecules are electrochemically reduced and split into carbon monoxide at the cathode side by applying external potential while the generated O^{2-} ions are transported though oxide-ion-conducting electrolyte to anode where pure oxygen is formed and released.

The Ni/YSZ composite electrode has been preferentially used as the cathode for oxide-ion-conducting solid oxide electrolysers for high-temperature electrolysis [4-6]. Mogensen *et al.* reported that the Ni/YSZ cermet was catalytically active for carbon dioxide electrolysis and claimed that it was feasible to conduct long-term CO_2 electrolysis on the Ni/YSZ electrode [7]. The catalytic activity of Ni metal toward the splitting of CO_2 is relatively high; carbon deposition most likely occurs and results in the degradation of cell performance. Some researchers have demonstrated that the deposition of carbon is likely caused by reactions that occur over the catalyst and favours to occur only when proper amount of CO is present in the chemical reaction system [7-8]. We have found that the mixture of CO_2/H_2O can quickly oxidize the Ni metal into amorphous phases composed of NiO and $Ni(OH)_2$ in the cathode that leads to cell performance degradation [9]. Compared with Ni/YSZ, the perovskite-type $La_xSr_{1-x}Cr_yMn_{1-y}O_{3-\delta}$ (LSCM) is an active and redox-stable material which can be used for high-temperature electrolysis and promising electrode performances have been obtained. As reported by Irvine *et al.*, the LSCM was successfully used as solid oxide electrolyser cathode for high-temperature steam electrolysis and promising performances was gained without reducing gas flowing over cathode [10-12]. Nevertheless, the p-type conduction mechanism of the LSCM is not well adapted to the strong reducing potential which leads to the conductivity drop, large electrode polarization resistances and cell performance degradation. We have also found that the current efficiencies of direct electrolysis of carbon dioxide based on LSCM cathode reached approximately 60% at low applied potentials and decreased rapidly at 2.0 V [13]. In contrast to LSCM, the perovskite $La_xSr_{1-x}TiO_{3+\delta}$ (LSTO) is an active and redox-stable material with high n-type conductivity upon reduction, which has been considered as the breakthrough in redox material for high temperature solid oxide fuel cells and solid oxide electrolysers [14-16]. However, the insufficient catalytic activity restricts the electrode polarization and current efficiency for high temperature electrolysis. We found that direct CO_2 electrolysis with a current efficiency of only 36% is achieved based on $La_{0.2}Sr_{0.8}TiO_{3.1}$ (LSTO) cathode at 700 °C with 2 V applied potential [17]. The impregnation of metal catalysts can effectively improve the performances of electrodes. However, it is difficult to control the morphology of catalysts; operation over a long time may lead to the agglomeration of catalysts and degrade the performances. We have also found that the steam electrolysis performances based on Ni-loaded LSTO are stable in the first few hours while the cell performances degrade approximately 20% after a long time test because of Ni particle agglomeration on electrode surface [18].

The other method is to incorporate the catalyst as a dopant within a host lattice under oxidizing conditions and partly exsolved to anchor the surface of matrix in the form of nanoparticles on subsequent reduction, which can be sufficient to avoid the agglomeration of catalyst nanoparticles on the substrate surface [19]. Cerium oxide is one of the most reactive rare earth metal oxides that have broad range applications in heterogeneous catalysis, electrochemistry and gas sensors [20-22]. The wide application of ceria and ceria-containing materials in heterogeneous catalysis is mainly due to the redox couple of Ce^{3+}/Ce^{4+} and its high capacity to oxygen storage [23-26]. Ceria is also used as the automotive three-way catalysts for reducing exhaust pollutants due to its high oxygen storage capacity [27]. Barnett *et al.* reported that the direct electrochemical oxidation of methane in solid oxide fuel cells based on ceria-containing anodes achieves promising performances which are ascribed to

the high ionic conductivity and the ability of readily storing and transferring oxygen [28]. Though the oxygen storage capacity is beneficial to heterogeneous catalysis, the electrocatalytic activity of ceria is still a limitation that restricts the overall electrode performances in contrast to conventional nickel metal. In contrast to single-metal oxide, the chemical behavior of mixed-metal oxides may be different as a consequence of two factors. On the one hand, the dopant can introduce stress into the lattice of ceria host and induce the formation of defects to balance the charge neutrality and modify chemical reactivity. On the other hand, the lattice of ceria can impose on the dopant element non-classical coordination modes with a subsequent perturbation in the dopant chemical properties. Wang *et al* reported the CuO_x/CeO_2 and $Ce_{1-x}Cu_xO_2$ catalysts for the WGS reaction and found that metallic copper and oxygen vacancies in ceria were involved in the generation of the catalytically active sites. The synergistic $Cu\text{-}O_{vacancy}$ interaction enhances the chemical activity of Cu, and the presence of Cu facilitates the formation of O vacancies in ceria [29]. The coupling of nanocatalysts and ceria substrates significantly enhance the heterogeneous catalytic activity because of the combination of the excellent catalytic activity of the nano-sized metal and the efficient accommodation/activation of reactant molecules in the oxygen-deficient sites on the substrate surfaces.

In this study, the $Ce_{1-x}Ni_xO_2$ (x=0, 0.05, 0.10, 0.15 and 0.20) catalysts are prepared using a combustion method. The nickel nanoparticles are exsolved to anchor ceria matrix to form heterogeneous catalysis sites through the combination of nickel nanocrystal and oxygen vacancies on ceria surfaces. The electrical properties of $Ce_{1-x}Ni_xO_2$ are systematically examined and direct carbon dioxide electrolysis with the new cathodes are performed and evaluated at intermediate temperatures.

Experimental

All chemicals utilized in this current investigation were of analytical grade unless otherwise specified. All the powders were purchased from SINOPHARM Chemical Reagent Co., Ltd (China). The $Ce_{1-x}Ni_xO_2$ (x=0, 0.05, 0.1, 0.15 and 0.2) powders were prepared by a combustion method [30] and denoted as CeNi0, CeNi5, CeNi10, CeNi15 and CeNi20, respectively. In the combustion method, $Ce(NO_3)_3{\cdot}6H_2O$ and $Ni(NO_3)_2$ were used as precursors. The required amounts of $Ce(NO_3)_3{\cdot}6H_2O$, $Ni(NO_3)_2$ and citric acid were dissolved in distilled water and stirred for 1 h at room temperature. Then the solution was transferred into a preheated furnace maintained at 500 °C for 5 minutes. The solution rapid dehydrated, burned and the grey colour solid product was obtained. The resulting powders were calcined in air at 800 °C for 3 h. The $(La_{0.8}Sr_{0.2})_{0.95}MnO_{3-\delta}$ (LSM) was prepared by a combustion method using glycine as fuel followed by a heat treatment at 1100 °C for 3 h in air. The $Ce_{1-x}Ni_xO_2$ samples were reduced in 5%H_2/Ar at 1000 °C for 3 h, respectively.

The phase formation of oxidized and reduced $Ce_{1-x}Ni_xO_2$ powders were confirmed using X-ray diffraction (XRD, Cu Kα, 2θ = 3°·min-1, D/MAX2500V, Rigaku Corporation, Japan). The microstructure of the oxidized and reduced CeNi10 were investigated by Scanning Electron Microscopy (SEM, SU8020, HITACHI Ltd, Japan) coupled with Energy Dispersive Spectroscopy (EDS). The morphological features were examined by SEM images under high vacuum (10^{-6} mbar), at 20 kV accelerating voltage and 90μA beam current. These regions were then examined by EDS, using a liquid N_2-cooled Si(Li) detector with a super-ultrathin Be window. Spectra were collected from six regions per surface employing area scan mode under 20 kV accelerating voltage, 110μA beam current and 500s acquisition time. Transmission Electron Microscopy analysis (TEM) was used to observe the oxidized and reduced CeNi10 powders with a JEOL 2100F field emission transmission electron microscope operated at 200 kV. X-ray photoelectron spectroscopy (XPS, ESCALAB25, Thermo, USA) was used to analyze the chemical states of the elements in the samples before and after high-temperature reduction. The Raman spectra were obtained on a confocal microprobe Raman system (LabRam HR Evolution, Horiba Jobin Yvon) with a laser excitation of wavelength of 532 nm. About 2.0 g CeNi0 and CeNi10 powders were pressed into a bar followed by sintering at 1400 °C and 1000 °C for 10 h in air, respectively. The relative density of CeNi0 and CeNi10 both reached approximately 80%. The conductivity was performed in air using the DC four-terminal method with temperature ranging from 200 to 800 ºC. The conductivity was recorded *versus* temperature using an online system at a step 0.5 °C from room temperature to 800 °C. The dependence of conductivity on oxygen partial pressure was tested at 800 ºC with the oxygen partial pressure ranging from 10^{-2} to 10^{-20} atm. The oxygen partial pressure was changed by flowing 5%H_2/Ar at the flow rate of 0.5 $mL{\cdot}min^{-1}$ controlled by a mass flow meter (D08-3F, Sevenstar, China). The oxygen partial pressure and conductivity were recorded using an online oxygen sensor (Type 1231, ZrO_2-based oxygen sensor, Noveltech, Australia) and an online multi-meter (Keithley 2000, Digital Multimeter, Keithley Instruments Inc., USA), respectively. About 1.5 g of CeNi0, CeNi5, CeNi10 and CeNi15 powders were pressed into disks with diameter of 20 mm followed by sintering at 1400, 1100, 1000 and 1000 ºC for 10 h to get samples for ionic conductivity tests, respectively. The ionic conductivities of the samples were tested in air using electron-blocking electrode method with temperature ranging from 200 to 800 ºC. The ionic conductivities were recorded with an online multi-meter (Keithley 2000, Digital Multimeter, Keithley Instruments Inc., USA).

A 2-mm-thick 8YSZ electrolyte support was prepared by dry-pressing 8YSZ powders into a green disk with a diameter of 20 mm followed by sintering in air at 1500 °C for 20 h. The two surfaces of YSZ electrolyte support were mechanically polished and ultrasonically cleaned in ethanol and distilled water. The $Ce_{1-x}Ni_xO_2$ slurries were prepared by milling the $Ce_{1-x}Ni_xO_2$ powders in the alpha-terpineol with appropriate amounts of cellulose additives. The composite LSM/YSZ slurries were prepared by milling YSZ powders with LSM powders at a weight ratio of 35:65 in the alpha-terpineol with the cellulose additive in a similar way. The symmetric electrolysers were prepared by printing the $Ce_{1-x}Ni_xO_2$ electrode slurries onto both surfaces of the YSZ electrolyte with an area of approximately 1 cm^2 followed by a heat treatment at 1100 ºC for 3 h in air. Silver paste (SS-8060, Xinluyi, Shanghai, China) was printed onto both surfaces of the electrodes to form current collector layer. The external circuit was made with silver wire (0.4 mm in diameter) which was fastened to current collectors using conductive adhesive (DAD87, Shanghai Research Institute for Synthetic Resins, Shanghai, China) followed by firing at 550 °C for 30 min in air. The single solid oxide electrolysers were prepared by coating LSM-YSZ on one side, whereas $Ce_{1-x}Ni_xO_2$ slurries were

coated on the other side followed by a heat treatment at 1100 ºC for 3 h in air. The symmetrical cells were tested at open circuit voltage (OCV) under different carbon monoxide partial pressure at 800 ºC using the electrochemical workstation (IM6, Zahner, Germany). The gas flow rate was controlled using a mass flow meter (D08–3F, Sevenstar, Beijing, China). The single solid oxide electrolysers were sealed to a home-made testing jig using ceramic paste (JD-767, Jiudian, Dongguan, China) for electrochemical measurements including AC impedance and current-voltage (I-V). The carbon dioxide electrolysis was performed at different applied voltages with carbon dioxide directly fed to cathode at 800 ºC. The output gas from the cathode was analyzed using an online gas chromatograph (GC9790II, Fuli, Zhejiang, China).

Results and discussion

Fig. 1 shows the XRD patterns of oxidized and reduced $Ce_{1-x}Ni_xO_2$ powders. As shown in Fig. 1, the results for both oxidized and reduced samples can be determined as fluorite structure with group of *Fm-3m* which is consistent well with the reported data in a previous work [31]. It can be seen in Fig. 1 (a), XRD patterns of CeNi5 and CeNi10 is single-phase which indicates the successful partial replacement of Ce^{4+} by Ni^{2+} in CeO_2. However, the characteristic peaks of NiO at 37.2 °, 43.3 ° and 62.8 ° appear for CeNi15 and CeNi20, which is in accordance with the solubility limit of a Ce-Ni exchange in ceria in the range of 10-12% [32]. Fig. S1 shows the cell parameters of $Ce_{1-x}Ni_xO_2$ (x=0, 0.05, 0.10, 0.15 and 0.20) calculated depending on the XRD data. It is observed that the cell parameters decrease from 5.413 Å to 5.394 Å when the proportion of nickel increases from 0 to 0.15. The introduction of Ni into CeO_2 lattice decreased the lattice parameter which is due to that the Ni^{2+} (0.69 Å) has a smaller ion radius than Ce^{4+} (0.97 Å) and introduces oxygen vacancy according charge balance. Fig. 1 (b) shows the XRD patterns of reduced $Ce_{1-x}Ni_xO_2$ samples, which confirms that the reduced $Ce_{1-x}Ni_xO_2$ (x=0.05, 0.10, 0.15 and 0.20) are mixture of two phases: CeO_2+Ni. As shown in Fig. 1 (b), the $Ce_{1-x}Ni_xO_2$ (x=0.05, 0.10, 0.15 and 0.20) change into CeO_2 and Ni upon high temperature reduction in 5%H_2/Ar and no phase transition is observed in the CeO_2 even after the high-temperature treatment in a very reducing atmosphere, firmly verifying superior redox stability of the ceria. The asymmetry of several peaks for the reduced samples d) and e) may be attributed to high concentration of oxygen vacancy. The asymmetry of XRD peaks is normally related to the distortion of XRD peaks [33]. The asymmetric peak shape is commonly observed for samples with significant concentration of defects [34]. G Neri *et al.* reported the Fe doped CeO_2 catalysts, as the Fe content increases, the diffraction peaks of the ceria become asymmetric which can be consequence of the decrease of the cell parameter due to an Fe^{3+} incorporation in the structure of CeO_2 [35]. In our work, the distortion of peak shape for 111, 220 and 311 peaks are probably due to the absorption because these two samples have the highest defect concentration after reduction.

Fig. 2 shows the high-resolution transmission electron microscopy (HR-TEM) analysis of the oxidized and reduced CeNi0 and CeNi10, respectively. As shown in Fig. 2 (a), the oxidized CeNi0 has revealed lattice spacing of 0.313(1) nm (111), which is consistent with the separation spacing determined by the XRD analysis. The lattice spacing of oxidized CeNi10 is 0.311(4) nm (111), which is nearly equal to that of the oxidized CeNi0, 0.313(1) nm (111). On the one hand, Ce^{4+} (0.97 Å) is partially replaced by Ni^{2+} (0.69 Å) in CeO_2 which may decrease the lattice parameter; On the other hand, the doping CeO_2 with Ni favors the formation of oxygen vacancy which makes a small expansion of the cell volume of CeNi10. The two effects cancel each other out and make the lattice spacing of oxidized CeNi10 has no obvious change. Fig. 2 (b) shows 0.323(6) nm (111) for the interplanar spacing of reduced CeNi0, which is larger than the oxidized CeNi0. This may due to that Ce^{4+} (0.97 Å) is the main chemical state in oxidized CeNi0 while the reduced CeNi0 contains a part of Ce^{3+} (1.14 Å) which may give rise to the lattice parameter expansion. It can be observed in Fig. 2 (d), the interplanar spacing of parent material CeO_2 is 0.321(5) nm (111) and the reduction of CeNi10 leads to growth of Ni nanoparticles on CeO_2 surface. The nickel has shown the interplanar spacing of 0.201(4) nm (111), which is consistent with the standard data of nickel data. The TEM results are in accordance with the results of XRD shown in Fig. 1. Fig. 3 shows the scanning electron micrographs (SEM) and energy-dispersive X-ray spectroscopy (EDS) maps taken from the oxidized and reduced CeNi10 pellets, respectively. The sintered samples were reduced in 5% H_2/Ar at 1200 °C for 6 hours. As shown in Fig. 3(a), the CeNi10 sample is dense and uniform without any microstructure deconstruction. Furthermore, the Ni element is homogeneously dispersed in oxidized CeNi10 sample and other elements are well distributed in the bulk. As shown in Fig. 3 (b), the nickel nanoparticles are uniformly exsolved from reduced CeNi10 sample and anchored on the CeO_2 surfaces. All the other elements are distributed evenly in the reduced sample. The SEM results further testify that the exsolved nickel nanoparticles anchor on the substrate surfaces and are consistent with the TEM and XRD results as discussed above. The well dispersed nickel nanoparticles anchoring on the CeO_2 surface may play an active role in prohibiting the agglomeration of nickel nanoparticles and improve the electrocatalytic activity of the electrode for high-temperature carbon dioxide electrolysis.

To confirm the elemental valence change, XPS analysis is performed to test the oxidized and reduced CeNi10 samples. All XPS dates are fitted using a Shirley-type background subtraction method, and the background functions for different spectra of the elements are fitted by 80% Gaussian and 20% Lorenz. Fig. 4 (a1) and (a2) show the Ce 3d core-level XPS results of oxidized and reduced CeNi10, respectively. The labels used for identifying Ce 3d XPS peaks follow the convention established by Burroughs *et al.* in which *u* and *v* indicate $3d_{5/2}$ and $3d_{3/2}$ spin-orbital components, respectively [36]. As shown in Fig. 4 (a1), the Ce^{4+} peaks contain u'''=916.58, u''=907.28, u=900.83, v'''=898.30, v''=888.57 and v=882.21 eV while Ce^{3+} peaks are observed at u'=903.91and v'=885.78 eV, respectively. The results indicate the Ce^{4+} is the dominated valence in oxidized CeNi10 sample. Fig. 4 (a2) shows that the Ce^{3+} peaks in reduced CeNi10 are stronger than the oxidized sample which is due to that parts of Ce^{4+} are reduced to Ce^{3+} after the heat treatment in a reducing atmosphere. Fig. 4 (b1) and (b2) show Ni 2p core level XPS spectroscopies of the oxidized and reduced CeNi10 samples, respectively. In Fig. 4 (b1), the Ni^{2+} $2p_{3/2}$ peaks are observed at 860.59, 855.50 and 853.71 eV. The Ni^0 peaks appear at 855.35 and 852.26 eV for the reduced sample as shown in Fig. 4 (b2), which further confirms the exsolution of metallic nickel on the CeO_2 surface. The signal

of Ni^{2+} is also observed in reduced sample which may be due to adsorption of atmospheric oxygen leads to the oxidation of nickel nanoparticles on the sample surface or tiny amount of nickel is still left in the CeO_2 lattice even after high-temperature reduction.

Fig. 5 shows the Raman spectra of $Ce_{1-x}Ni_xO_2$ (x=0, 0.05, 0.10 and 0.15). The samples show a brand with high intensity at approximately 460 cm^{-1} and a weak band at 1172 cm^{-1}, which are ascribed to the F_{2g} vibration mode and A_{1g} asymmetry mode in metal oxide with a fluorite structure, respectively [37-38]. For the $Ce_{1-x}Ni_xO_2$ (0.05, 0.10 and 0.15) catalysts, the spectra are dominated by a strong band associated with the F_{2g} vibration mode, which shifts to lower frequencies compared with CeO_2 substrate, suggesting the successful formation of $Ce_{1-x}Ni_xO_2$ solid solution with Ni^{2+} replacing Ce^{4+} in CeO_2 lattice. All samples display a weak brand at approximately 590 cm^{-1}, which has been widely reported to be the defect-induced D band that is strongly associated with oxygen vacancies [39-40]. It should be also noted that the intensity of the D band at about 590 cm^{-1} increases with increasing Ni content, which further indicates that the oxygen vacancy concentration in the $Ce_{1-x}Ni_xO_2$ is influenced by the amount of substitution of Ce^{4+} by Ni^{2+}. The CeNi15 has the strongest intensity of the D band at about 590 cm^{-1} indicating the maximum concentration of oxygen vacancy.

In order to study the electrical properties of CeNi0 and CeNi10, conductivity tests were performed in air *versus* temperature (20–800 °C) and oxygen partial pressure (pO_2) at 800 °C. Fig.6(a) shows that the conductivities of CeNi0 and CeNi10 improve with temperature, which demonstrates a typical p-type semiconducting behavior. In air, the charge carrier is hole that is generated by the combination of oxygen vacancy and atmospheric oxygen. The conductivity of CeNi10 is higher than CeNi0 because of part of Ce^{4+} is replaced by Ni^{2+} leading to the oxygen vacancy concentration increased. However, the oxidized CeNi0 and CeNi10 show low conductivities in air even at high temperature. The redox activity of CeO_2 materials is expected to improve the electronic conductivity in stronger reducing atmosphere. As shown in Fig. 6 (b), the total conductivity of CeNi10 is higher in the region of high pO_2, but lower in the extreme reducing atmospheres, which indicates that the dopant of Ni increases ionic conductivity but simultaneously reduces electronic conductivity. The conductivities of CeO_2 materials are significantly enhanced at low pO_2 because of the reduction cerium cations from 4+ to 3+ state that contributes to the n-type conduction of the reduced CeO_2 materials. The conductivity of CeNi10 is comparable with CeNi0 at the pO_2 of 10^{-18} atm due to the exsolution of nickel nanoparticles anchoring on the substrate surfaces without forming connected Ni network. The ionic conductivity test was conducted using DC polarization method with temperature ranging from 20 to 800 °C [41-42]. The configuration of the cell with electron blocking is YSZ/$Ce_{1-x}Ni_xO_2$/YSZ. The Ag paste was painted on the outside of both the connected samples an YSZ pellets as current collectors. The electron flux is blocked by YSZ layer because YSZ is considered to be a pure oxide-ion conductor. Glass seal was used to prevent oxygen leakage along the sides of the samples. A DC voltage is applied on the outside of both samples and YSZ layers and stable current can be observed at designated temperature. Fig. 7 shows the temperature dependence of ionic conductivity of the oxidized $Ce_{1-x}Ni_xO_2$ (x=0, 0.05, 0.10 and 0.15) in air from 400 to 800 °C. The ionic conductivities of oxidized $Ce_{1-x}Ni_xO_2$ (x=0, 0.05, 0.10 and 0.15) improve with both temperature and nickel doping content. The ionic conductivities of CeNi0, CeNi5, CeNi10 and CeNi15 finally reach 7.663×10^{-5}, 2.549×10^{-4}, 4.876×10^{-4} and 7.851×10^{-4} S•cm^{-1} at 800 °C, respectively. The doped Ni in $Ce_{1-x}Ni_xO_2$ lattice increases oxygen vacancy concentration and therefore significantly improves the ionic conductivities.The ionic conductivity of CeNi15 is 1 order of magnitude higher than CeNi0, which may be ascribed to the absence of sufficient oxygen vacancy as the charge carrier for the ionic transport.

Fig.8 shows the AC impendence spectra of the symmetric solid oxide cells with electrodes based on $Ce_{1-x}Ni_xO_2$ (x=0, 0.05, 0.10, 0.15 and 0.2) at different carbon monoxide partial pressure under OCV condition at 800 ºC, respectively. The series resistance (R_s) and the polarization resistance (R_p), depicted by the first intercept and the difference between the first and second intercepts, are calculated by Zview software as reported in our previous work [43]. The R_s of the symmetrical cells are generally stable in a wide range of carbon monoxide partial pressure. As shown in Fig. 8 (a), the R_p based on CeO_2 decreases from approximately 11.5 to 6.5 $\Omega\cdot cm^2$ with carbon monoxide partial pressure ranging from 0 to 5%. Similar behavior has also been observed for CeNi5, CeNi10, CeNi15 and CeNi20 electrode in symmetric cells, respectively. The R_p decreases from 11.3 to 4.0 $\Omega\cdot cm^2$, 7.5 to 3.4 $\Omega\cdot cm^2$, 4.5 to 1.5 $\Omega\cdot cm^2$ and 5.3 to 2 $\Omega\cdot cm^2$, respectively. The results suggest that stronger reducing atmosphere is beneficial to electrode polarization improvement. For $Ce_{1-x}Ni_xO_2$ (x=0, 0.05, 0.10 and 0.15), the polarization resistance gradually decreases with increasing the content of nickel. However, the R_p of the symmetric cell based on CeNi20 is higher than CeNi15 which may be due to the high nickel content leads to the nickel agglomeration which degrades the electrode performances.

Fig. 9 shows the current-voltage curves for the direct carbon dioxide electrolysis based on the solid oxide electrolysers with $Ce_{1-x}Ni_xO_2$ (x=0, 0.05, 0.10, 0.15 and 0.20) cathodes, respectively. The slope change of the I-V curves occurs at approximately 1.0 V which is the onset voltage of electrolysis indicating that there exist two different cell processes in the voltage regions: one is the electrochemical reduction of the cathodes and oxidation of the anode at low voltage; the other is the carbon dioxide electrolysis at high voltages. The maximum current density reaches 0.245, 0.275, 0.330, 0.391 and 0.345 $A\cdot cm^{-2}$ at 2.0 V for the electrolysers with CeNi0, CeNi5, CeNi10, CeNi15 and CeNi20 cathodes, respectively. The current density increases with Ni content which is ascribed to the synergistic effects of catalytic-active Ni particles and oxygen-deficient substrate that forms heterogeneous electrocatalytic sites in $Ce_{1-x}Ni_xO_2$ (0.05, 0.10, 0.15 and 0.20) cathodes. Fig. 10 shows the *in-situ* AC impedance spectroscopy under a series of applied voltages ranging from 1.2 to 2.0 V at 800 ºC with CeNi0, CeNi5, CeNi10, CeNi15 and CeNi20 cathodes, respectively. It is observed that the R_s values are stabilized at approximately 2.5 $\Omega\cdot cm^2$; however, the R_p values sharply decreases as applied voltage increases from 1.2 to 2.0 V, which may be attributed to the fact the applied voltage not only activates the electrode but also electrochemically reduces the electrode to enhance the mixed conductivity and electrocatalytic activity. The R_p based on CeNi0 cathode drops

from 3.0 to 1.0 $\Omega \cdot cm^2$ when the applied voltage ranges from 1.0 to 2.0 V. Similar behavior has also been observed for CeNi5, CeNi10, CeNi15 and CeNi20 electrodes under the same conditions, respectively. Here, the R_p decreases from 2.00 to 0.50 $\Omega \cdot cm^2$, 1.25 to 0.45 $\Omega \cdot cm^2$, 1.0 to 0.38 $\Omega \cdot cm^2$ and 1.1 to 0.44 $\Omega \cdot cm^2$, respectively. It is very clear that the presence of nickel nanocatalyst can effectively improve the electrode-catalytic activity of the electrodes and accordingly reduce the electrode polarization resistances in accordance with results of the symmetrical cells tests as shown in Fig. 8. Fig. S2 shows the R_p *versus* i.R corrected voltages for the direct carbon dioxide electrolysis. These data allow further understanding the polarization changes under different voltages where the voltages of i.R are subtracted. It can be seen that the voltage at 1.6 V between two electrode is sufficient to electrochemical reduce the cathode. Fig.11 shows the rate of carbon monoxide production and current efficiency of the electrolysers *versus* the $Ce_{1-x}Ni_xO_2$ (0, 0.05, 0.10, 0.15 and 0.20) cathodes for carbon dioxide electrolysis with the applied voltage of 1.4, 1.6 and 1.8 V, respectively. As shown in Fig. 11 (a), the carbon monoxide production rates improve with increasing the applied voltages. The maximum carbon monoxide production rates with $Ce_{1-x}Ni_xO_2$ (0, 0.05, 0.10, 0.15 and 0.20) cathodes are 0.811, 1.166, 1.334, 1.757 and 1.526 $ml \cdot min^{-1} \cdot cm^{-2}$ at 1.8 V, respectively, which are about two times higher than the carbon monoxide productions at 1.4 V. It should be also noted that the production rate of carbon monoxide is dependent on the content of nickel in $Ce_{1-x}Ni_xO_2$ solid solution. Fig. 11 (b) shows the current efficiencies with x in $Ce_{1-x}Ni_xO_2$ (0, 0.05, 0.10, 0.15 and 0.20) cathodes. The current efficiencies improve with increasing the nickel content and applied voltages. For $Ce_{1-x}Ni_xO_2$ (0, 0.05, 0.10 and 0.15), the current efficiencies improved obviously with the nickel content ($0 \le x \le 0.15$). However, the current efficiencies of CeNi20 (71.1, 77.1 and 82.8%) are a little higher than CeNi15 (68.1, 75.8 and 80.8%) at 1.4, 1.6 and 1.8 V, respectively, which confirms the optimum nickel content in CeNi15 cathode for the improved electrode performances.

In order to further validate the electrode performances of CeNi15 and CeNi20 cathodes, direct carbon dioxide electrolysis was performed at a fixed voltage of 1.4 V at 800 °C for 30 h. As shown in Fig. 12 (a), the current density of CeNi15 has a little drop in the first 5 h and it appears to keep a stable level from 6 to 30 h. However, a sharp drop of the current density of CeNi20 happens in the initial 5 h and finally decays about 20%, and then becomes stable from 6 to 30 h. The initial cell performance degradation with CeNi20 may be due to nickel nanoparticle agglomeration. However, the cell performances appear to be stable after running for a longer time. Similar trend in current efficiency has also been observed as shown in Fig. 12 (b). The current efficiency with CeNi15 reaches 68% and demonstrates a stable trend even after 30 h test; however, the current efficiencies with CeNi20 decays at initial 5 h and finally stabilize at 66%. The combination use of XRD, TEM, SEM and XPS confirms the *in-situ* growth of Ni nanocatalysts to anchor onto the CeO_2 surface which can prevent the agglomeration of nickel nanoparticles. As shown in Fig. 13 and Fig. 14, the nickel particles uniformly distribute in CeNi15 cathode without obvious change before and after test. In contrast, excess nickel particles agglomerate on the surface of CeNi20 after carbon dioxide electrolysis test as shown in Fig. 14 (b).

Conclusions

In this work, $Ce_{1-x}Ni_xO_2$ (0, 0.05, 0.10, 0.15 and 0.20) were prepared and characterized for high temperature carbon dioxide electgrolysis. The *in-situ* growth of Ni catalysts to anchor on the CeO_2 substrate has been successfully achieved and utilized for effectively improving electrode activity. The ionic conductivity and electro-catalytic properties improve with increasing Ni content. Efficient carbon dioxide electrolysis is then achieved using CeNi15 and CeNi20 cathodes. However, obvious performance degradation for the CeNi20 cathode is observed because of the Ni nanoparticle agglomeration. While CeNi15 shows the highest ionic conductivity and best electrochemical performances for carbon dioxide electrolysis at high temperature. All results indicate that the synergistic effects of catalytic-active Ni nanoparticles and oxygen-deficient substrate with heterogeneous electrocatalytic sites may be an effective choice for enhancing high-temperature carbon dioxide electrolysis in an oxide-ion conducting solid oxide electrolyser.

Acknowledgements

This work is financially supported by the Natural Science Foundation of China (NSFC) No. 21303037, China Postdoctoral Science Foundation No. 2013M53150, the Ministry of Education of Overseas Returnees Fund No.20131792 and the Fundamental Research Funds for the Central Universities No. 2012HGZY0001.

Affiliations

[a] *School of Materials Science and Engineering, Hefei University of Technology, No.193 Tunxi Road, Hefei, Anhui 230009, China. Email: xiekui@hfut.edu.cn; ycwu@hfut.edu.cn.*

[b] *Key Laboratory of Advanced Functional Materials and Devices, Hefei University of Technology, No.193 Tunxi Road, Hefei, Anhui 230009, China.*

References

1 R. Lan, S.W. Tao, J.T.S. Irvine, *Energy Environ. Sci.*, 2013, 3,438-441.
2 F. Bidrawn, G. Kim, G. Corre, J. T. S. Irvine, J. M. Vohs, R. J. Gorte, *Electrochem.Solid State Lett.*, 2008, 11, B167-B170.
3 T. Ishihare, N. Jirathiwathanakul, H. Zhong, *Energy Environ. Sci.*, 2010, 3, 665-672.
4 W. T. Qi, Y. Gan, D. Yin, Z. Y. Li, G. J. Wu, K. Xie, Y. C. Wu, *J. Mater. Chem. A*, 2014, 2, 6904-6915.
5 A. hauch, S. D. Ebbesen, S. Jensen, M. Mogensen, *J. Mater. Chem.*, 2008, 18, 2331-2340.
6 C. Graves, S.D. Ebbesen, M. Mogensen, *Solid State Ionics*, 2011, 192, 398-403.
7 S. D. Ebbesen, M. Mogensen, *J. Power Sources*, 2009, 193, 349-358.
8 F. Bidrawn, G. Kim, G. Corre, J. T. S. Irvine, J. M. Vohs, R.J. Gortea, *Electrochem. Solid St.*, 2008, 11, B167-B170.
9 G. J. Wu, K. Xie, Y. C. Wu, W. T. Yao, J. Zhou, *J. Power Sources*, 2013, 232, 187-192.
10 X.D. Yang, J.T.S. Irvine. *J. Mater. Chem.*, 2008, 18, 2349-2354.
11 S. W. Tao, J. T. S. Irvine, *Nat. Mater.*, 2003, 2, 320-323.
12 Y. Gan, J. Zhang, S.S. Li, K. Xie, J. T. S. Irvine, *J. Electrochem. Soc.*, 2012, 159, F763-767.

13 S.S. Xu, S.S. Li, Y, Gan, Y.X. Li, K. Xie, *J. Power Sources*, 2013, 230, 115- 121.
14 G. Tsekouras, D. Neagu, J. T. S. Irvine, *Energy Environ. Sci.*, 2013, 6, 256-266.
15 D. Neagu, J. T. S. Irvine , *Chem. Mater.*, 2010, 22, 5042-5053.
16 K. Xie, Y. Q. Zhang, G. Y. Meng, J. T. S. Irvine, *Energy Environ. Sci.*, 2011, 4, 2218-2222.
17 Y. X. Li, Y. Gan, S. S. Li, Y. Wang, H. F. Xiang, K. Xie, *Phys Chem Chem Phys*, 2012,14, 15547-15553.
18 Y. Gan, Q. Q. Qin, S. G. Chen, Y. Wang, D. H. Dong, K. Xie, Y. C. Wu, *J. Power Sources*, 2014, 245, 245-255.
19 D. Neagu, G. Tsekouras, D. N. Miller, H. Ménard, J. T. S. Irvine, *Nature Chemistry*, 2013, 5, 916-923.
20 J. Guzman, S. Carrettin, A. Corma, *J. Am. Chem. Soc.*, 2005, 127, 3286-3287.
21 S. Park, J. M. Vohs, R. J. Gorte, *Nature*, 2000, 404, 265-267.
22 L. Liao, H. X. Mai, Q. Yuan, H. B. Lu, J. C. Li, C. Liu, C. H. Yan, Z. X. Shen, T. Yu, *J. Phys. Chem. C*, 2008, 112, 9061-9065.
23 Y. M. Chiang, E. B. Lavik, I. Kosacki, H. L. Tuller, J. Y. Ying, *Appl. Phys. Lett.*, 1996, 69 ,185-187.
24 S. W. Zha, W. Rauch, M. L. Liu, *Solid State Ionics*, 2004, 166, 241-250.
25 S. W. Zha, A. Moore, H. Abernathy, M. L. Liu, *J. Electrochem. Soc.*, 2004, 151, A1128-A1133.
26 T. Masui, K. Fujiwara, K. I. Machida, G. Y. Adachi, *Chem.Mater.*, 1997, 9, 2197-2204.
27 V. G. Milt, C. A. Querini, E. E. Miró, M. A. Ulla, *J. Catal.*, 2003, 220, 424-432.
28 E. P. Murray, T. Tsai, S. A. Barnett, *Nature*, 1999, 400, 649-651.
29 X. Q. Wang, J. A. Rodriguez, J. C. Hanson, D. Gamarra, A. Martínez-Arias, M. Fernández-García, *J. Phys. Chem. B*, 2006, 110, 428-434.
30 S. Mahammadunnisa, P. M. K. Reddy, N. Lingaiahb, C. Subrahmanyam, *Catal. Sci. Technol.,* 2013, 3, 730-736.
31 N. Yisup, Y. Cao, W. L. Feng, W. L. Dai, K. N. Fan, *Catal. Lett.*, 2005, 99, 207-213.
32 G. Zhou, L. Barrio, S. Agnoli, S. D. Senanayake, J. Evans, A. Kubacka, M. Estrella, J. C. Hanson, A. Martínez-Arias, M. Fernández-García, J. A. Rodriguez, *Angew. Chem.*, 2010, 122, 9874-9878.
33 H. J. Wang, J. Zhou, *J. Appl. Crystallogr.*, 2000, 33, 1128-1135.
34 H. J. Wang, J. Zhou, *J. Appl. Crystallogr.*, 2000, 36, 1133-1136.
35 G. Neri, A Pistone, C. Milone, S. Galvagno, *Appl. Catal. B-Environ*, 2002, 38, 321-329.
36 P. Burroughs, A. Hamnett, A. F. Orchard, G. Thornton, *J. Chem. Soc., Dalton Trans.*, 1976, 17, 1686-1698.
37 G. Vlaic, R. D. Monte, P. Fornasiero, E. Fonda, J. Kaspar, M. Graziani, *J. Catal.*, 1999, 182, 378-389.
38 W. H. Weber, K. C. Hass, J. R. Mcbride, *Phys. Rev. B*, 1993, 48,178-185.
39 J. R. Mcbride, K. C. Hass, B. D. Poindexter, W. H. Weber, *J. Appl. Phys.*, 1994, 76, 2435-2441.
40 B. M. Reddy , A. Khan , P. Lakshmanan, *J. Phys. Chem. B*, 2005, **109**, 3355-3363.
41 X. Li, H. L. Zhao, F. Gao, Z. M. Zhu, N. Chen, W. Shen, *Solid State Ionics*, 2008, 179, 1588-1592.
42 A. Endo, M. Ihara, H. Komiyama, K. Yamada, *Solid State Ionics*, 1996, 86-88, 1191-1195.
43 Y. X. Li, G. J. Wu, C. Ruan, Q. Zhou, Y. Wang, W. Doherty, K. Xie, Y. C. Wu, *J. Power Sources*, 2014, 253, 349-359.

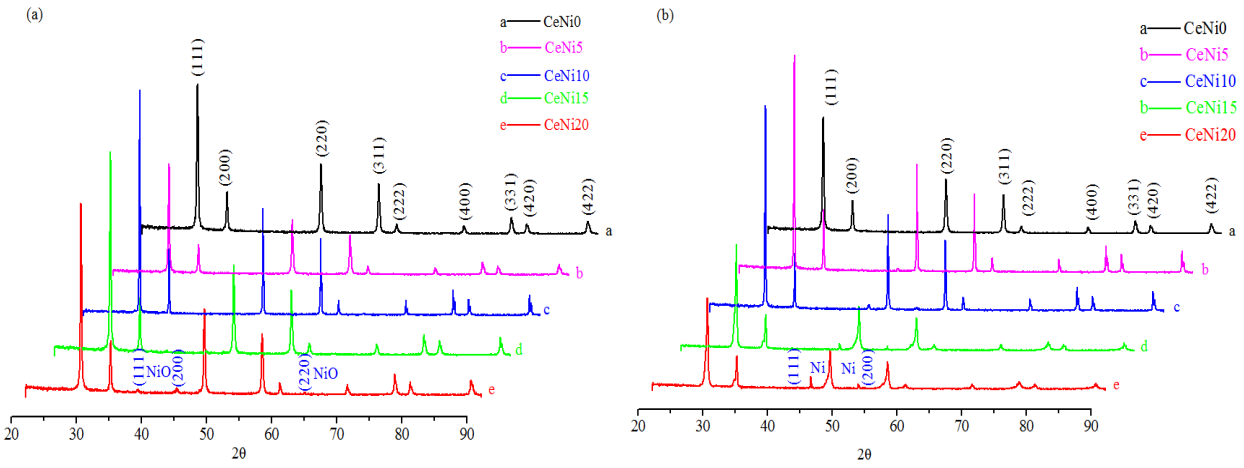

Fig. 1: XRD pattern of $Ce_{1-x}Ni_xO_2$ (0, 0.05, 0.10, 0.15 and 0.20) (a: the patterns of the oxidized form; b: the patterns of the reduced form).

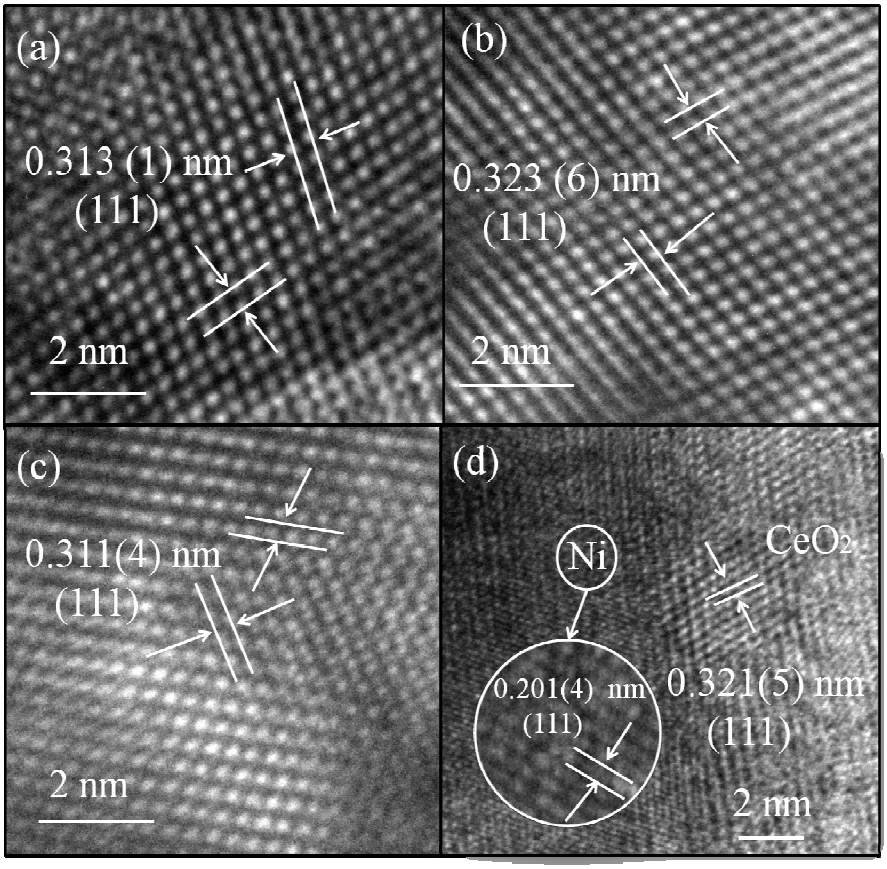

Fig. 2: The TEM graph of the oxidized CeNi0 (a), reduced CeNi10 (b), oxidized CeNi10 (c) and reduced CeNi10 (d).

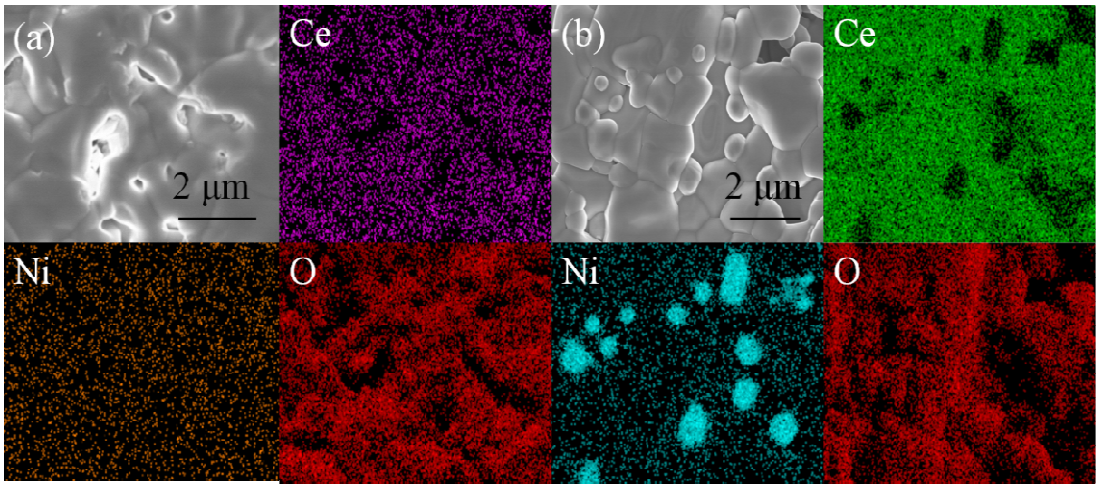

Fig. 3: SEM and EDS results of the oxidized form of CeNi10 (a) and the reduced form of CeNi10 (b).

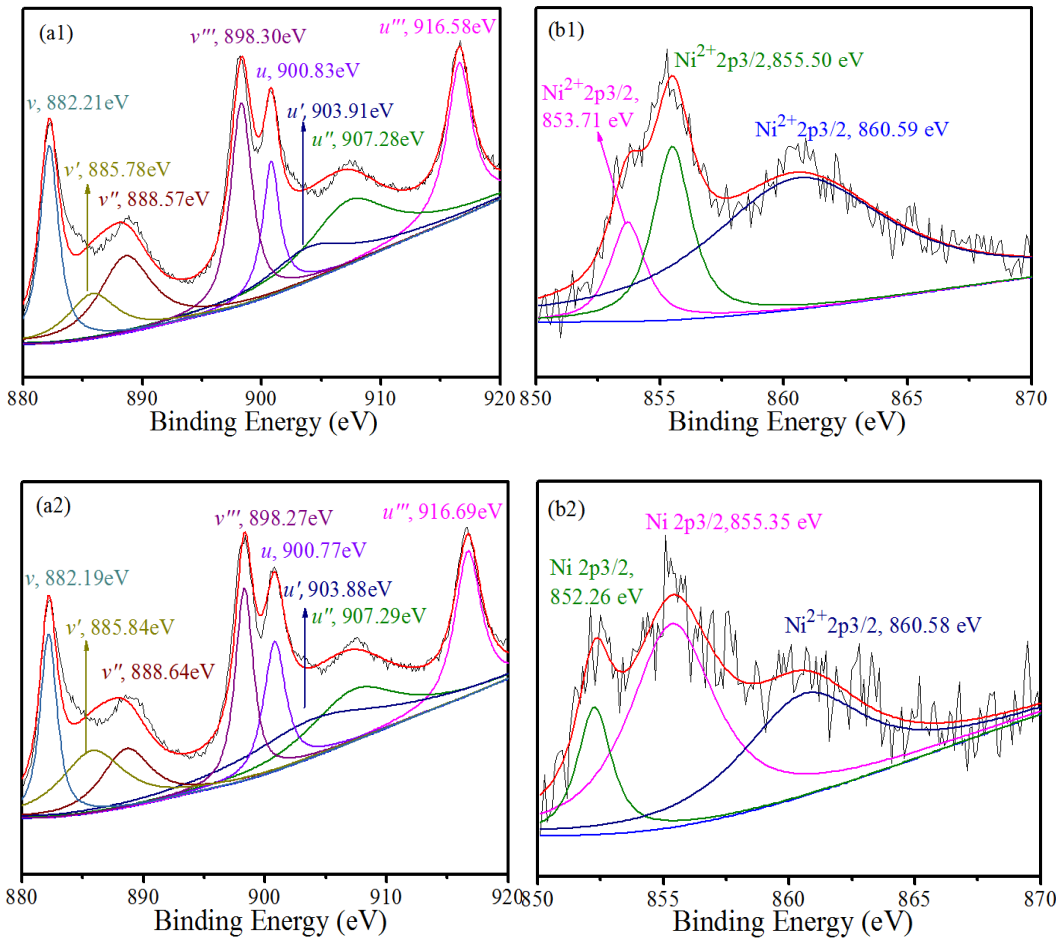

Fig. 4: XPS results of Ce (a1) and Ni (b1) in the oxidized CeNi10; Ce(a2) and (b2) in the reduced CeNi10.

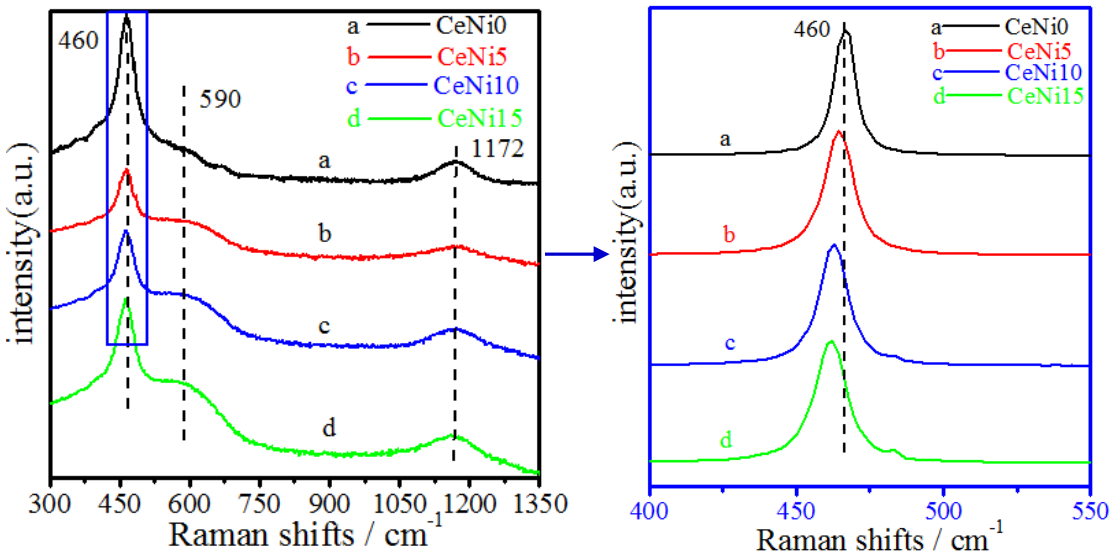

Fig. 5: The Raman spectra of $Ce_{1-x}Ni_xO_2$: a, x=0; b, x=0.05; c, x=0.10; d, x=0.15.

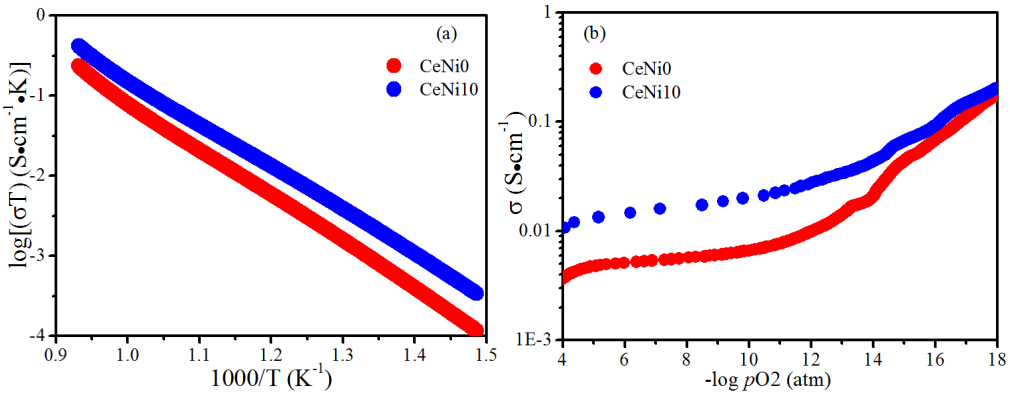

Fig. 6: (a) The dependence of conductivity on temperature of the oxidized form of CeNi0 and CeNi10 samples; (b) the dependence of the conductivity on oxygen partial pressure of the oxidized form of CeNi0 and CeNi10 samples at 800 ºC.

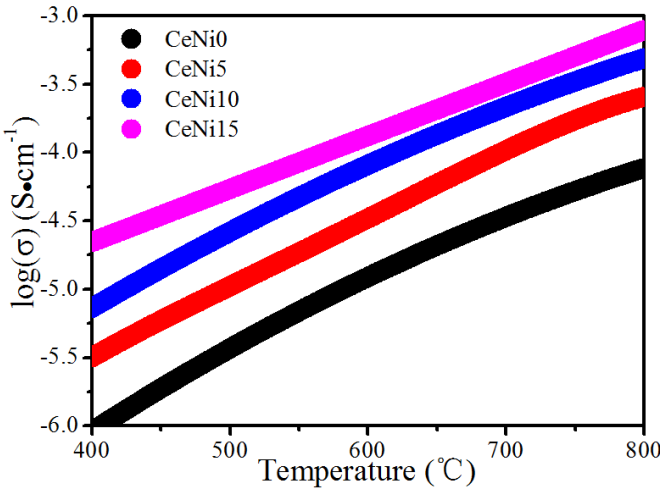

Fig. 7: The dependence of ionic conductivities on temperature of the oxidized $Ce_{1-x}Ni_xO_2$ (0, 0.05, 0.10 and 0.15) in air.

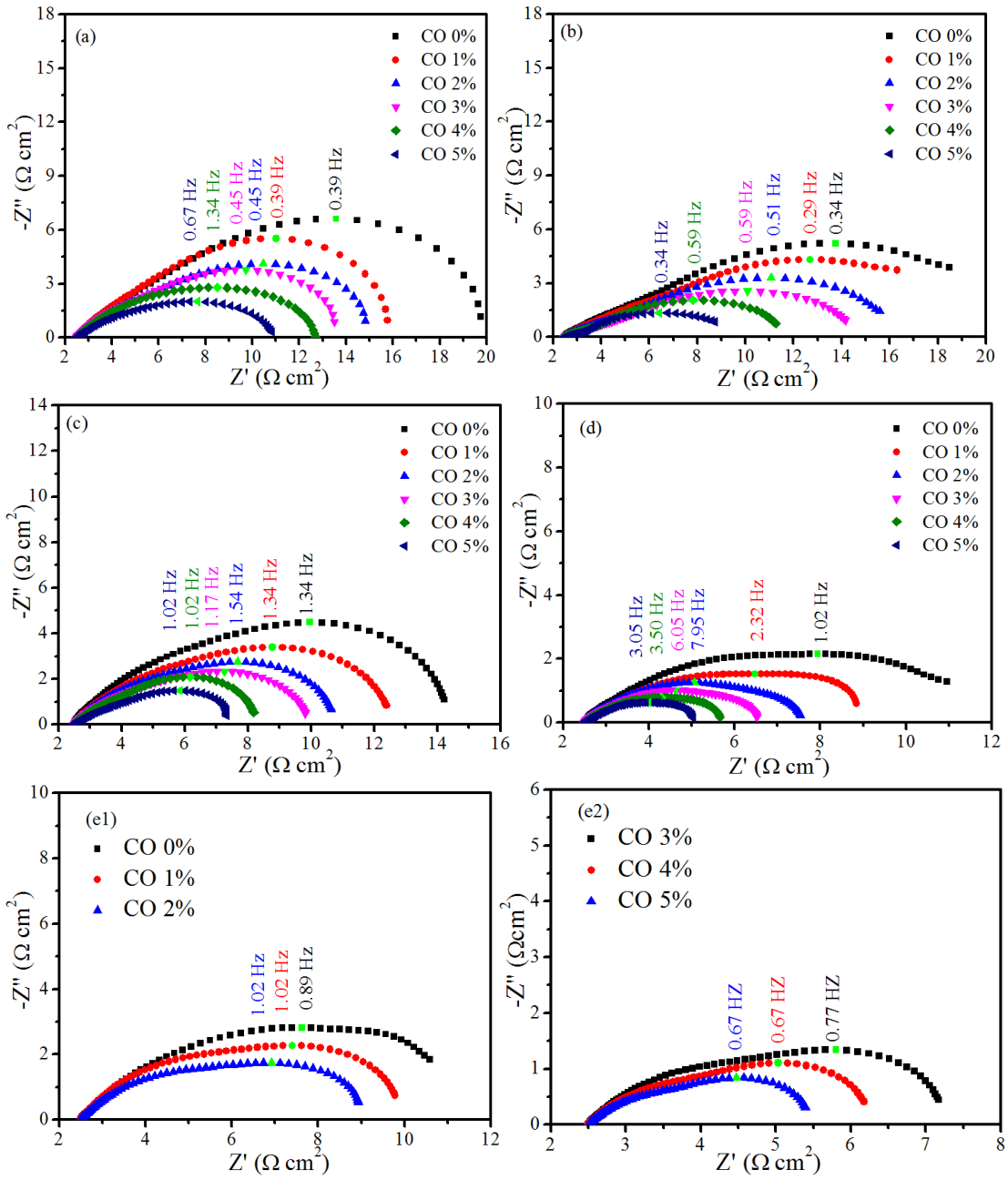

Fig. 8: AC impendence of the symmetrical cells based on $Ce_{1-x}Ni_xO_2$ electrode with x=0 (a) x=0.05 (b), x=0.10 (c), x=0.15 (d) and x=0.20 (e1, e2) tested at 800 °C with different carbon monoxide partial pressures.

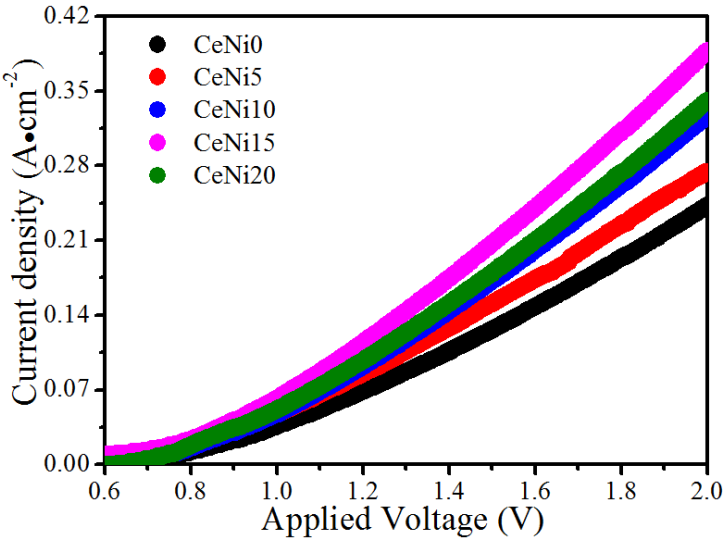

Fig. 9: I-V curve of the solid oxide electrolyzers based on $Ce_{1-x}Ni_xO_2$ (0, 0.05, 0.10, 0.15 and 0.20) cathodes for CO_2 electrolysisat 800 ºC.

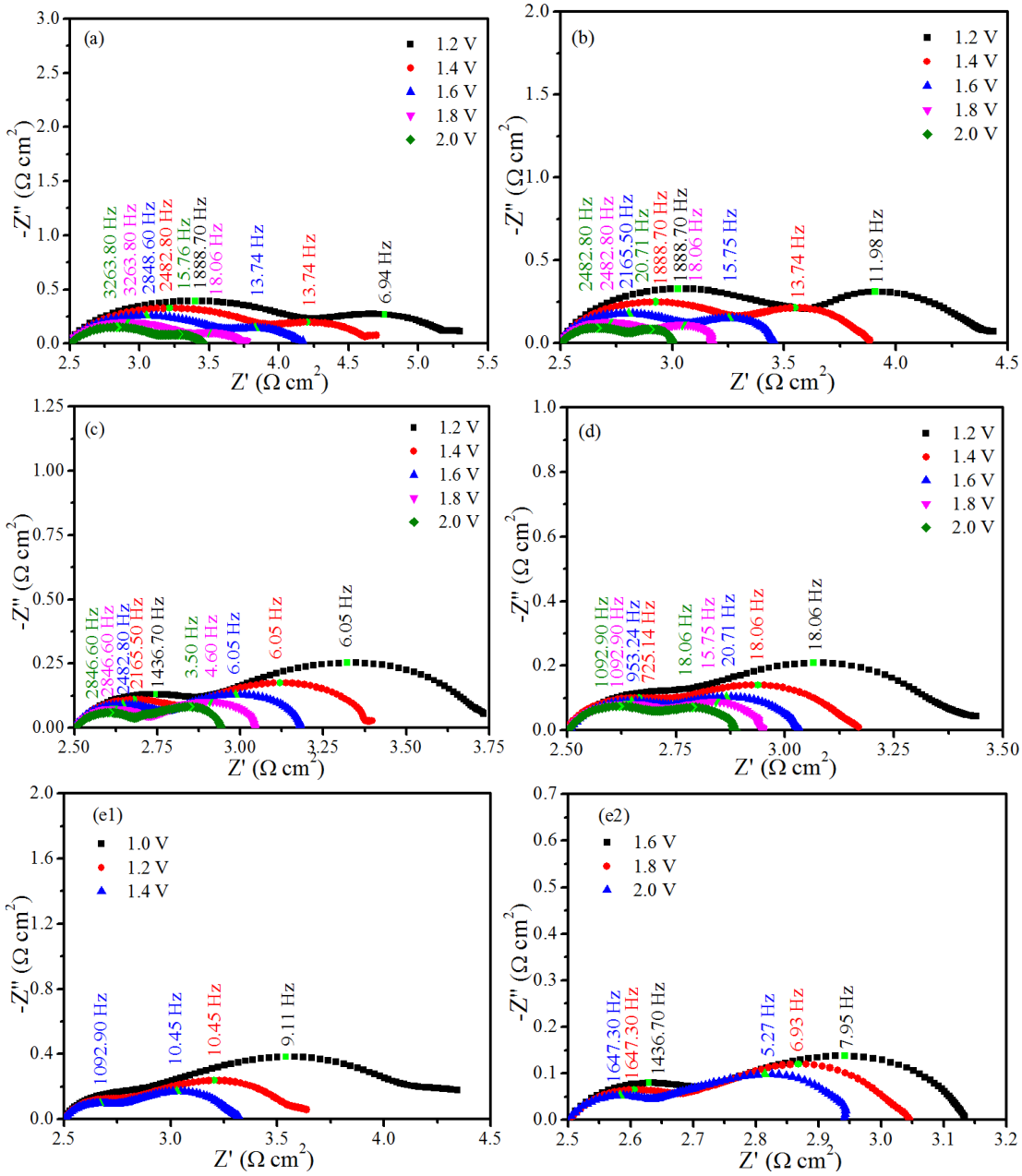

Fig. 10: AC impendence of the solid oxide electrolyzers based on $Ce_{1-x}Ni_xO_2$ electrode with x=0 (a) x=0.05 (b), x=0.10 (c), x=0.15 (d) and x=0.20 (e1, e2) for CO_2 electrolysis at 800 ºC.

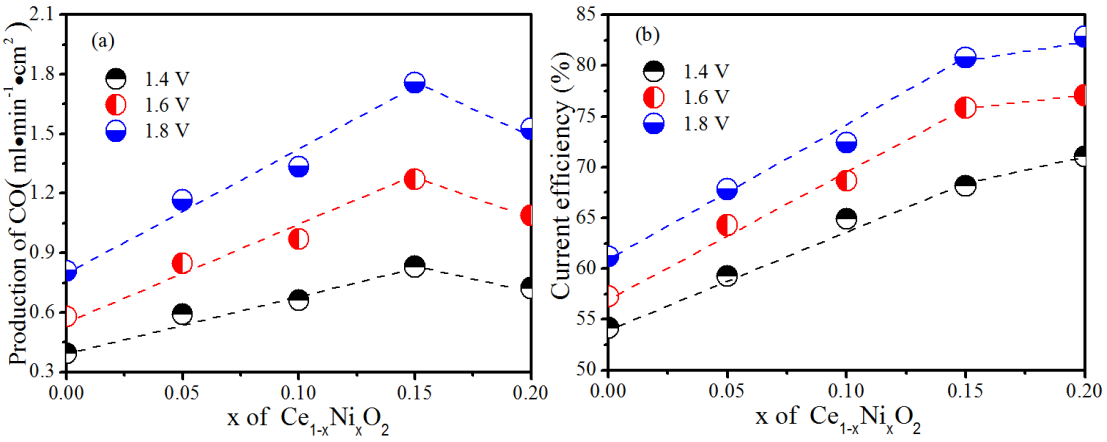

Fig. 11: (a) The CO production rate for the cells based on $Ce_{1-x}Ni_xO_2$ (0, 0.05, 0.10, 0.15 and 0.20) composite cathode *versus* x of $Ce_{1-x}Ni_xO_2$; (b) the relationship between the current efficiency of the CO2 electrolysis and x in the $Ce_{1-x}Ni_xO_2$ (0, 0.05, 0.10, 0.15 and 0.20) composite cathodes.

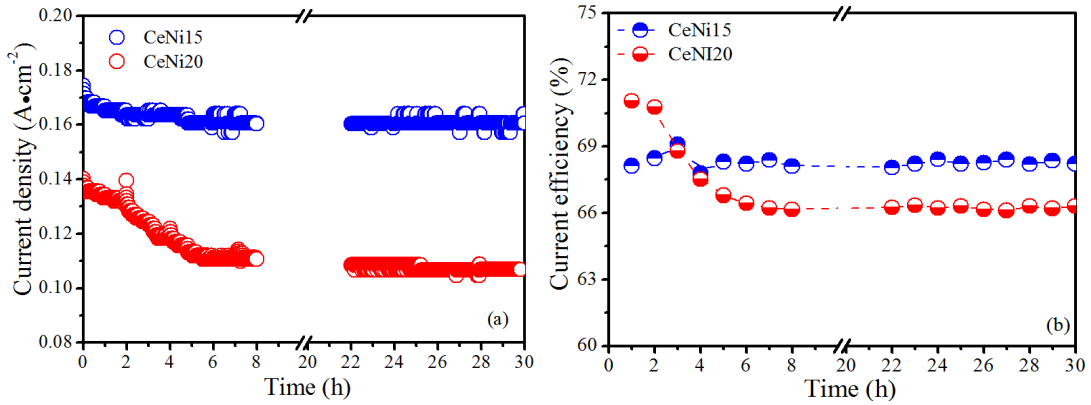

Fig. 12: Short-term performance of the electrolyzer with CeNi15 and CeNi20 cathode at 800 ºC under 1.4 V for carbon dioxide electrolysis: (a) the change of current density; (b) the change of current efficiency.

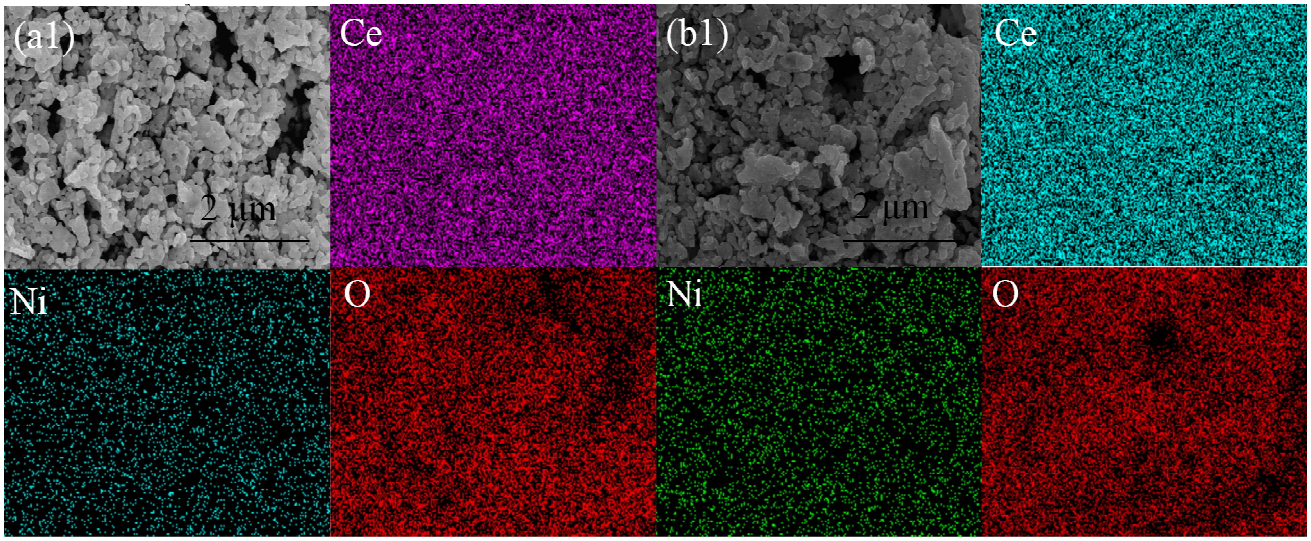

Fig. 13: SEM and EDS of CeNi15 (a) and CeNi20 (b) cathodes before the carbon dioxide electrolysis test.

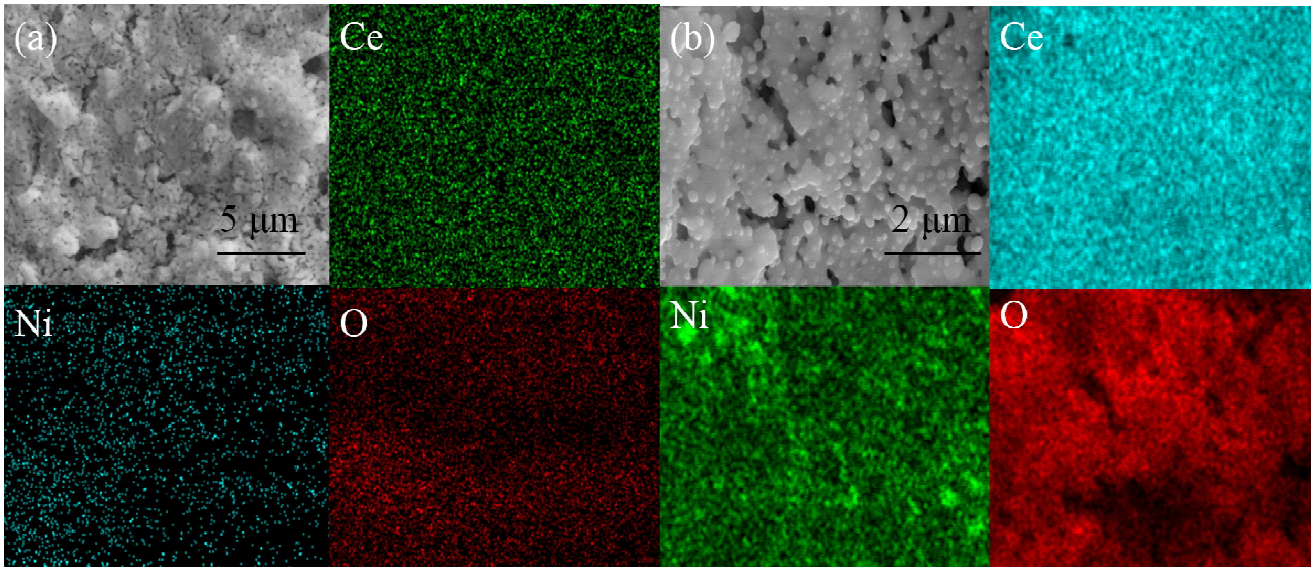

Fig. 14: SEM and EDS of CeNi15 (a) and CeNi20 (b) cathodes after the carbon dioxide electrolysis for 24 h.